Published in final edited form as:
IEEE Trans Biomed Circuits Syst. 2010 June 14; 4(5): 301–. doi:10.1109/TBCAS.2010.2049491.

Optimization of Data Coils in a Multiband Wireless Link for Neuroprosthetic Implantable Devices

Uei-Ming Jow[Student Member, IEEE] and **Maysam Ghovanloo[Student Member, IEEE]**
GT Bionics Lab, School of Electrical and Computer Engineering, Georgia Institute of Technology, Atlanta, GA 30308 USA

Uei-Ming Jow: jow0209@gatech.edu; Maysam Ghovanloo: mghovan@ece.gatech.edu

Abstract

We have presented the design methodology along with detailed simulation and measurement results for optimizing a multiband transcutaneous wireless link for high-performance implantable neuroprosthetic devices. We have utilized three individual carrier signals and coil/antenna pairs for power transmission, forward data transmission from outside into the body, and back telemetry in the opposite direction. Power is transmitted at 13.56 MHz through a pair of printed spiral coils (PSCs) facing each other. Two different designs have been evaluated for forward data coils, both of which help to minimize power carrier interference in the received data carrier. One is a pair of perpendicular coils that are wound across the diameter of the power PSCs. The other design is a pair of planar figure-8 coils that are in the same plane as the power PSCs. We have compared the robustness of each design against horizontal misalignments and rotations in different directions. Simulation and measurements are also conducted on a miniature spiral antenna, designed to operate with impulse-radio ultra-wideband (IR-UWB) circuitry for back telemetry.

Index Terms

Cross coupling; figure-8 coils; multiband inductive wireless link; neuroprostheses; telemetry

I. Introduction

WIRELESS operation of implantable microelectronic devices (IMD) is necessary in clinical neuroprostheses to reduce the risk of infection and patient discomfort, which may result from transcutaneous wires breaching the skin. This requirement, however, adds to the complexity of the system and may form a bottleneck in the design of high-performance IMDs that are being developed for new applications, such as retinal implants and cortical brain-machine interfaces (BMI). Even though the transmission range of these wireless links is limited to 5 ~ 20 mm across the skin, the medium (tissue) and extreme size constraints may require the adoption of nontraditional design criteria. For example, cochlear implants need to be placed inside the 3- to 6-mm-thick temporal bone near the ears [1], and invasive BMIs are being developed for the 1- to 3-mm epidural spacing between the outer surface of the brain and the skull [2]. Moreover, the retinal implants are expected to be placed inside the eyeball through a 5-mm incision [3], [4].

The wireless link is expected to perform three functions as follows.

This paper was recommended by Associate Editor A. Mason.

1. Power transmission: Design and optimization of efficient inductive power transmission links with filament coils have been studied over the last decades [5]–[9]. Nonetheless, the geometry of the coils used in the next generation of low-power IMDs is more likely to be planar and lithographically defined, to allow fabrication through micromachining technology [10]. Therefore, we devised an iterative design methodology to find key geometric parameters of the planar spiral coils (PSC) and maximize their power transmission efficiency in [11].
2. Forward data transmission: Prostheses that substitute for sensory modalities, such as vision, need large volumes of data to simultaneously stimulate a large number of sites at high rates [12]. Thus, wideband wireless data transmission from outside into the body (downlink) is needed. Due to conflicting requirements between power and data links, we have utilized a separate pair of coils for data transmission [13]. In this paper, we consider two types of data coils. First, there are a pair of vertical coils wound across the diameter of the power PSCs, whose symmetry and orthogonal magnetic-field orientation will minimize the power carrier interference. Second, a pair of planar figure-8 coils, in which the electromotive force (EMF) induced from the power carrier in one loop, opposes the same in the other loop [14]. Hence, the total electromotive-force (emf) interference from the power carrier can be very small when the two coils are properly aligned.
3. Back telemetry: Recording the neural response to stimulation in neuroprostheses and closing the control feedback loops in the BMIs require a wideband back telemetry link (uplink). Passive back telemetry, used in radio-frequency identification (RFID), does not provide enough bandwidth for this application [15], or requires strong coupling between coils [16]. Therefore, we chose impulse-radio ultra-wideband (IR-UWB) for this purpose, which can provide wide bandwidth with simple and low-power transmitters [17]. We have included a pair of planar spiral UWB antennas in our multiband wireless link. However, we have not yet optimized it at this stage.

Fig. 1 shows the block diagram of a high-performance neuroprosthetic device, which has wireless neural recording and stimulation capabilities, with emphasis on the proposed multiband wireless link. The upper, middle, and lower rows in this diagram are responsible for power, forward data, and back telemetry functions, respectively. L_1 is the external power PSC that is attached to the skin from outside of the body and L_2 is the internal PSC that is implanted under the skin flap. L_3 and L_4 are the forward data coils. The back telemetry link utilizes miniature UWB antennas A_1 and A_2.

In Section II, we construct a theoretical foundation for data coils. The design procedure and optimization of the multiband wireless link components are discussed in Section III. The theory and design of the power PSCs have already been covered in [11] and [18]. Section IV is dedicated to simulation and measurement results, followed by concluding remarks.

II. Theoretical Calculations for Data Coils

A. Vertical Data Coil

The geometry and orientation of the forward data coils are key issues because the power carrier amplitude can be up to two orders of magnitude larger than the data carrier, and can easily dwarf the data carrier particularly on the receiver side. A coaxial approach has been proposed, in which data coils are placed in the center of the power coils in the same plane [19]. This approach provides good coupling between data coils (k_{34} in Fig. 1). However, $L_1 \sim L_4$ all share the same flux linkage, resulting in a strong cross coupling between these coils, which can lead to saturation of the data receiver by strong power carrier interference.

Although a high-pass filter on the receiver side can reduce the power carrier interference up to a certain extent, in our experience, the power carrier is so strong that only a high-order filter with large area and power costs might be effective. Even then, the inband harmonic components of the power carrier cannot be neglected. Hence, unless the interference between the power and data carriers is adequately attenuated on both sides, demodulation of the received data carrier and correct detection of the data bits would be difficult.

To solve this problem, we proposed using orthogonal coils by winding the data coils across the diameter of the power PSCs, as shown in Fig. 2 [13]. In this method, due to symmetry and orthogonality of the coils' geometries, the magnetic flux generated by the power PSCs does not pass through data coils and their undesired cross coupling factors (k_{14}, k_{13}, k_{23}, and k_{24}) can theoretically be close to zero when the coils are perfectly aligned. The data coils, however, can maintain a small but adequate direct coupling k_{34} as they are parallel with long conductors.

One should note that unlike power PSCs, which need strong coupling (k_{12}) to efficiently supply the IMD, here we only need to maintain k_{34} in the same range or slightly higher than the undesired couplings. Since the forward data link operates at a different frequency band, the receiver L_4C_{P4} tank helps with amplifying the received data carrier and filtering out the undesired power carrier interference [13]. In the following text, we have constructed a theoretical foundation to optimize the geometries of the vertical data coils.

In Fig. 2, the height (h_d), width (w_d), and length (l_d) of each rectangular vertical data coil depend on the thickness of the power PSC substrate, number of turns of data coil (N_d), and the diameter of the power PSC, respectively. w_d also depends on the diameter of the chosen wire (*Dia*) and their spacing. Using these geometrical parameters in tabular self inductance formulation in [5], we calculated L_3 and L_4 (see the Appendix).

The coupling coefficient between a pair of coils is defined as

$$k_{34}=M_{34}/\sqrt{L_3L_4} \tag{1}$$

where M_{34} is the mutual inductance between L_3 and L_4. Fig. 3 shows the cross section of the rectangular solenoid-shaped data coils. We showed in [13] that vertical data coils are quite robust against misalignments along the Y-axis (see Fig. 2), and sensitive to misalignments along the X-axis. Therefore, to derive M_{34} equations, we not only considered the coils relative distance D, but also their X-axis misalignment X. The original equations for the mutual inductance from [5] were based on circular solenoids. We used the rectangular coil height (h_d) instead of the circular solenoid diameter. We also replaced the area of the circular solenoid by the rectangular solenoid area ($l_d \times h_d$). Our simulation and measurement results showed that these approximations are valid for $l_d/h_d < 20$. Detailed equations for calculating M_{34} from data coil geometries are included in the Appendix.

B. Figure-8 Data Coils

Our second design for the data coils is based on the planar figure-8 geometry, shown in Fig. 4(a). This type of coil is often used in transcranial magnetic stimulation (TMS) [21]. The direction of windings in each loop of the coil is chosen so that when the coil is exposed to an external field symmetrical to both loops, induced currents will cancel each other out [22]. Therefore, even when they are in the same plane as the power PSCs, figure-8 coils can attenuate the power interference. Moreover, the mutual coupling M between two figure-8 data coils is larger than that between vertical coils because these coils are facing each other.

We dedicated two out of four metal layers in the printed-circuit board (PCB) implementation of the multiband link to the figure-8 data coils with $N_{d3} = N_{d4} = 2$ [see Fig. 4(b)]. We made L_4 as large as the IMD size allowed (i.e., filling the same area as L_2). Geometry, line width, and substrate thickness affect the self inductance and the mutual coupling of the figure-8 coils. Since closed-form equations for figure-8 coils are quite complicated, we used a commercial field solver, HFSS (Ansoft, Pittsburgh, PA), to model these parameters.

III. Multiband Wireless Link Design Procedure

A. Printed Spiral Power Coils

Theoretical analysis, modeling, and experimental validation of an iterative design procedure for the power PSCs based on a set of constraints imposed by the fabrication process and medical application can be found in [11]. We combined the theoretical foundation of optimal power transmission in inductive links with simple models that calculate M in a pair of PSCs, their quality factors (Q), and parasitic components. The result was an iterative PSC design methodology that starts with a set of realistic design constraints imposed by the application and PSC fabrication process, and ends with the optimal PSC geometries for maximum power efficiency.

Table I summarizes the constraints that we have considered in the design of the prototype power transmission PSCs for an exemplar visual prosthesis application, using 1-oz copper on FR4 substrate in a standard PCB fabrication process. We executed the iterative procedure for $f_P = 13.56$ MHz in the industrial scientific medical (ISM) band and nominal coupling distance of $D = 10$ mm. Even though 13.56 MHz is on the high end of the frequencies that have been traditionally adopted for inductive power transmission to implantable devices, it is still within the range in which the specific absorption rate (SAR) in the tissue is quite low compared to the thermal power dissipation in the coils [24]–[27]. On the other hand, it provides high-Q for L_1 and L_2, which is a key factor in improving the power transmission efficiency [28]. It also allows us to take advantage of the existing radio-frequency identification (RFID) technology. Table II depicts the optimized geometries for L_1 and L_2.

B. Vertical Data Coils

Optimal forward data coil geometries depend on the choice of the forward data carrier frequency. In this prototype, we chose a phase-coherent frequency-shift-keyed (pcFSK) carrier at $f_{FD1} = 25$ and $f_{FD0} = 50$ MHz based on the method described in [23]. Fig. 2(a) shows the main geometrical parameters of the data coils (l_d, w_d, h_d, n_d). In order to reduce thickness and the skin effect, we chose the thinnest multistrand Litz wires that we could find for winding the vertical data coils (MWS Wire Industries, Westlake Village, CA). This wire had a diameter of $Dia_4 = 100$ μm, including insulation, which contained seven insulated strands of AWG-48 wires (diameter ~ 30.5 μm).

Fig. 5 summarizes our three-step design procedure for vertical data coils. To maximize k_{34}, we would like l_{d4} to be as long as possible. Therefore, the first constraint is imposed by the size of the IMD, which is basically the size of L_2 [11]. Using Table II, $l_{d4} = d_{o2} + 2Dia_4 =$ 10.2 mm. The height of L_4 (i.e., h_{d4}) is dictated by the IMD thickness with $2Dia_4$ which is 1.7 mm in this case. Increasing n_{d3} and n_{d4} improves k_{34} at the expense of decreasing the data coils' self resonant frequency (SRF) and increasing undesired k_{14} and k_{23}. SRF is defined as

$$\mathrm{SRF}=1/2\pi\sqrt{\mathrm{LC}}, \tag{2}$$

where L is the coil's self-inductance and C is its parasitic capacitance. The closer the SRF gets to the carrier frequency, the smaller the size of the added parallel or series capacitance needs to be with the data coil inductor (C_{p4} and C_{s3}). Therefore, it becomes more difficult to tune the LC resonance frequency right at the desired carrier frequency because we have little control over C. Hence, as a rule of thumb, we try to keep SRF at least twice the carrier frequency, which means $C \leq C_{p4}/3$. SRF should not be too high either. In order to increase SRF, one has to reduce n_{d3} and n_{d4} at the cost of reducing k_{34}.

Considering the aforementioned discussion, in our example, we would like to choose n_{d3} and n_{d4} so that $SRF_{3,4} \geq 100$ MHz. Even though there are closed-form equations for the SRF of solenoid air-core inductors [29]; in this case, L_3 and L_4 are wound around $L_1$and L_2, respectively, which degrade the accuracy of these equations. Hence, in Fig. 6, we used HFSS to simulate the relationship between SRF and n_{d4} for a single-strand rectangular coil with $l_{d4} = 10.2$ mm, $h_{d4} = 1.7$ mm, $w_{d4} = 1$ mm, and $Dia_4 = 100\ \mu$m. It can be seen that for $n_{d4} = 6$, $SRF_4 = 96.3$ MHz. Measurements with the 7-strand Litz wire and same dimensions resulted in $SRF_4 = 98.8$ MHz.

In the second step, since dimensions of L_1 and L_4 as well as their relative distance D are known, we can simulate k_{14} using the field solver to determine the power carrier interference. D in this case is considered the distance between the closest conductors in L_1 and L_4. Our simulation with HFSS resulted in $k_{14} = 9.1 \times 10^{-5}$ at 25 MHz, which is the minimum value for k_{14} when the coils are perfectly aligned. However, since the interference can be through multiple paths, the best alignment can be found by shifting L_4 horizontally about 0.5 mm in each direction from the center of the power coil until minimum power interference from f_P is achieved. In the next step, we would like to design L_3 so that k_{34} is at least one order of magnitude larger than k_{14}.

l_{d3} (length of L_3) plays an important role in k_{34} value. A short l_{d3} turns L_3 into a solenoid with concentrated magnetic field but smaller cross section. If l_{d3} is too long, on the other hand, L_3 turns into a series of infinite parallel conductors with respect to L_4 with lower mutual coupling. Hence, there is an optimal length for l_{d3}. To demonstrate the effect of l_{d3} on k_{34}, we simulated k_{34} between L_4 (from step 1) and an $n_3 = 3$-, 5-, and 10-turn L_3, while sweeping l_{d3} from 10 ~ 70 mm. Once again, $D = 10$ mm, and h_{d3} was set to 2.2 mm (PCB thickness with $2Dia_3$), where $Dia_3 = 350\ \mu$m which is a reasonable thickness (we will discuss it latter). The results in Fig. 7 show that $l_{d3} = 30$ mm is the optimal length for L_3 in these conditions.

Dia_3 and n_{d3} are the other parameters that need to be determined in this step, which have direct relationships with k_{34}. From the previous step, $l_{d3}/h_{d3} \approx 17.6 < 20$. Hence, the models and equations discussed in Section II are valid. Using (3)–(5) in the Appendix, we have created Fig. 8 in MATLAB by sweeping Dia_3 and n_{d3} from 0 to 0.5 mm and 0 to 10 turns, respectively. Despite their positive effect on k_{34}, increasing Dia_3 will add to the thickness of the external coil/antenna complex, and increasing n_{d3} will reduce SRF_3. To wind L_3, we decided to use Litz wires with $Dia_3 = 350\ \mu$m, made of seven insulated AWG-36 strands (diameter ~ 127 μm). This type of wire, indicated by a dashed line in Fig. 8, adds ~ 700 μm to the 1.5-mm-thick L_1, which is reasonable for outside the body.

To find the proper n_{d3}, we simulated SRF_3 with all the known geometrical parameters of L_3, while sweeping n_{d3} from 1 to 10. It can be seen in Fig. 6 that $n_{d3} = 5$ would be the best choice, resulting in $SRF_3 = 128.8$ MHz. This point has been shown by a red dot in Fig. 8, corresponding to $k_{34} = 0.00246$, which is 27 times larger than simulated k_{14}. This concludes with the optimal vertical data coils design, whose specifications are summarized in Table III for $D = 10$ mm.

C. Figure-8 Data Coils

Fig. 4(a) shows the figure-8 data coil (L_4) geometry. Note that the two loops are laid out symmetrically with opposite winding directions. Similar to the vertical data coils, the largest possible area for L_4 is dictated by the IMD size, which is the size of L_2 (d_{o4} = 10 mm). We chose the line width for L_4 to be 200 μm, slightly larger than the minimum widths possible in our PCB fabrication process. Layers 2 and 3 of a four-layer FR4 PCB are dedicated to the implantable figure-8 data coil, which are spaced at 0.8 mm [see Fig. 4(b)]. The simulated SRF_4 with the aforementioned dimensions was 256 MHz.

To find the best size for L_3, we learned from [15] that the optimal radius of a 1-turn circular loop for maximum coupling with another loop that has a radius of R at distance D is ~ $D\sqrt{2}$, when R is small. Since $D = R$ =10 mm in our design, we chose the size of L_3 to be 32 × 32 mm^2, which is slightly larger than the optimal size to account for the width of the planar conductors. The line width affects not only the parasitic resistance but also SRF_3. We chose a line width of 2 mm on a 2-layer 1.5-mm-thick PCB, and achieved SRF_3 = 138 MHz in simulations. Specifications of our figure-8 data coil designs are summarized in Table IV.

D. UWB Antenna

Wideband antennas are often composed of several resonant frequencies [30]. To cover the lower bands, a long antenna is needed to be efficient for long wavelengths. However, with the limited space available in the implant, another choice could be to use a high dielectric substrate to create lower resonant frequencies at shorter wavelengths. Unfortunately, a 10 × 10 mm^2 lossy FR4 substrate is not a suitable choice for either one of the aforementioned solutions. Therefore, we do not expect a great performance from our antenna pair $A_1$and A_2 in Fig. 1. Fortunately, that is not a major issue because of the proximity of the two antennas across the skin. In order to reduce the size, spiral antennas can be used [31], [32]. Even then, dedicating only one metal layer for this antenna is not enough to create a low resonance frequency. Thus, we took advantage of the power coil as the ground plane to create another radiation path and lower the resonance frequency of the antenna further.

A_2 consists of seven turns of planar copper with the line width of 400 μm and line spacing of 200 μm on the backside of L_2. The feedpoint of this 10 mm in diameter UWB antenna is at the center. A key advantage of this planar design is that it can be batch fabricated on a thin organic substrate with minimum volume overhead in an actual IMD. However, we still need to improve the design of this antenna based on its specific conditions inside the body [33], [34]. Fig. 4(b) shows an exploded view of the entire multiband coil-antenna complex on a four-layer PCB. A_1 is not under a strict size constraint, and can be an elliptical dipole antenna, filling the area on the back of L_1. The operating principle between A_1 and A_2 is considered near-field coupling (5 ~ 20 mm). However, the short-range impulse radio UWB communication, which we will utilize for back telemetry [35], is much less susceptible to misalignments compared to the forward data coils.

IV. Measurement and Simulation Results

The measurement setup is shown in Fig. 9. We connected the coils under test to a 4-GHz vector network analyzer (R&S ZVB4) in pairs to measure their S-parameters. S-parameters were then converted to Z-parameters to calculate the quality factors and mutual inductances [36]. We finally used (1) and equations in [11] to calculate the coupling coefficients and efficiency, respectively. Since optimal $d_{o1} > l_3$ (see Tables II and III), in order to wind L_3 we had to create a pair of holes in L_1 PCB and pass the Litz wire through them (see Fig. 9 inset). More detail on the power efficiency setup can be found in [11].

A. Power Coils Efficiency

Fig. 10 shows the measured efficiency of the power PSCs in Table II versus coils relative distance D at 13.56 MHz, and compares it with HFSS simulations and calculations based on the models we constructed in [11]. The calculated, simulated, and measured results are in good agreement. The small discrepancies of the calculated values result from the fact that the equations in [11] were mainly for circular coils and we empirically adjusted them for the rectangular-shaped PSCs by adding a simple coefficient. Furthermore, we did not take into account the effects of eddy currents in those equations.

B. Data Coils Linear Misalignments

One of the key issues in forward data transmission using a multiband wireless link is its robustness against misalignments. Here, because we have previously shown that these coils are robust against misalignments along the Y-axis [13], we focus on misalignment along the X-axis [see Fig. 2(a)]. Fig. 11(a) shows the result of k_{14} and k_{34} variations at $D = 10$ mm when vertical data coils in Section III-B are misaligned up to 10 mm along the X-axis. It can be seen that the desired k_{34} appears well above the undesired interference from power PSCs (k_{14}) in perfect alignment ($\Delta X = 0$ mm) and $k_{34} > k_{14}$ for $\Delta X < 2.5$ mm. Therefore, we can conclude that this design can generally withstand misalignments of up to 2.5 mm for the 10 × 10 mm^2 implant (~25% of the implant size).

A similar set of experiments was conducted with figure-8 data coils of Section III-C, and the results in Fig. 11(b) show that k_{14} and k_{34} of figure-8 coils are stronger than k_{14} and k_{34} of the vertical data coils when the coils are perfectly aligned. In this design, however, $k_{34} > k_{14}$ for $\Delta X < 8$ mm. Thus, we can conclude that this design can withstand misalignments of up to 8 mm for the 10 × 10 mm^2 implant (~80% of the implant size).

C. Data Coil Rotations

Due to coils' proximity, even small rotations affect their coupling coefficients considerably. In this section, simulations and measurements of the vertical and figure-8 data coils' k_{34} versus the rotation angle are shown in Fig. 12(a) and (b) based on the Cartesian coordinates shown in Figs. 2(a) and 4(b), respectively. In these measurements, L_4 is held stationary and L_3 is rotated pivotal to X-, Y-, and Z-axes, while the center-to-center spacing between the coils is maintained at $D = 10$ mm.

According to Fig. 12(a), the rotations along X- and Y-axes actually increase k_{34} in the vertical data coils. In figure-8 coils, however, all rotations result in k_{34} reductions. Nevertheless, without considering the changes in k_{14}, we cannot draw any conclusions about the effects of rotations. k_{14} was too small to be shown in the same scale as k_{34}. Hence, we considered k_{34}/k_{14} as a figure of merit (FoM) to compare the data coil designs.

D. Comparison of Data Coils

Fig. 13(a) and (b) shows k_{34}/k_{14} versus linear misalignments and rotations, respectively. The level at which $k_{34}/k_{14} = 1$ is a good measure for indicating how much misalignment or rotation can be handled by each coil design. Fig. 13(a) shows that when the coils are perfectly aligned, the vertical data coils are in a stronger position. However, they are affected by X-axis misalignment more rapidly than figure-8 coils. According to Fig. 13(b), vertical data coils are more robust against rotations pivotal to X- and Z-axes compared to figure-8 coils. In rotations larger than 10° pivotal to the Y-axis, however, figure-8 coils are stronger, because this type of rotation affects the orthogonal advantage of the vertical data coils and increases their exposure to power PSCs magnetic flux [see Fig. 2(a)].

E. Power PSC and Data Coils Cross Coupling

So far, we have only considered the interference from the power carrier onto the received data carrier directly through k_{14}. By inspecting Fig. 1, however, one can see that there are two other possible paths for this interference. One is the coupling from L_1 onto L_2 (the power link) and then from L_2 onto L_4. This can be represented by $k_{12} \times k_{24}$. The other is from L_1 onto L_3 and then from L_3 onto L_4 (the forward data link), which can be represented by $k_{13} \times k_{34}$. Between these two, we expect $k_{12} \times k_{24} > k_{13} \times k_{34}$ because of the strong coupling between L_1 and L_2 (k_{12}). To understand the significance of these undesired coupling paths, particularly when the coils are misaligned, we have compared all three paths versus X-axis misalignments in Fig. 14 through simulation and measurements. Fig. 14(a) shows that in vertical data coils, even though $k_{12} \times k_{24}$ and $k_{13} \times k_{34}$ are comparable to k_{14} in perfect alignment ($k_{14} = 3.9 \times 10^{-5}$ versus $k_{12} \times k_{24} = 1.1 \times 10^{-5}$), they remain at about two orders of magnitude below k_{34}, while k_{14} grows rapidly as a result of X-axis misalignment [compared with Fig. 11(a)]. Therefore, we do not need to be concerned about these indirect interference paths in vertical data coils.

Fig. 14(b) shows the same comparison for figure-8 data coils. In this case, $k_{13} \times k_{34}$ is very small and can be ignored. However, k_{14} and $k_{12} \times k_{24}$ are close in perfect alignment ($k_{14} = 6.8 \times 10^{-4}$ versus $k_{12} \times k_{24} = 4.0 \times 10^{-4}$), and $k_{12} \times k_{24}$ remains smaller but comparable to k_{14}. One possible way of taking advantage of $k_{12} \times k_{24}$ is to make sure that its sign is opposite that of k_{14}. This is possible with the proper selection of the direction of windings in L_1 and L_2. This leads to the power carrier interference through $k_{12} \times k_{24}$ to be out of phase with the main source of interference through k_{14} and slightly weakens it.

F. UWB Antennas

Antennas are typically characterized by their radiation pattern, directivity, efficiency, gain, and bandwidth, and all of these characteristics are affected by their environment [33], [34]. However, in this work, we only measured the S_{11}, the return loss, in the air to observe the radiation bandwidth. Fig. 15 shows the simulation and measurement results for the S_{11} of the planar spiral UWB antenna A_2, stacked on top of the power PSC and figure-8 data coils in a 4-layer PCB as shown in Fig. 4(b). It can be seen that the UWB antenna has a radiation bandwidth from 2.5 to 5 GHz with $S_{11} < -10$ dB, which is expected to be sufficient for transmitting tens of megabits per second of recorded data across a short distance (5 ~ 20 mm) by using the IR-UWB technique [37].

Fig. 15 also shows the S_{11} when we added the vertical data coil to the Fig. 4(b) combination, as seen in Fig. 2(b). The vertical data coil affected the frequency response of the antenna, and the 2.5 ~ 5 GHz window was no longer available. Therefore, the spiral UWB antenna design needs to be modified if it is intended to be used with vertical data coils. It should also be noted that at high frequencies, electromagnetic power absorption in the tissue increases the antenna losses, and true evaluation of these antenna designs should be done in saline or appropriate tissue simulants [38], [39]. Therefore, more work is needed to develop IR-UWB antennas that are optimized specifically for the ground-plane geometry (PSC), the choice of data coils, and the surrounding environment.

V. Conclusion

We have presented a novel method for the design and optimization of a multiband wireless link that has a dedicated carrier signal and a coil/antenna pair for every major function that is expected from the wireless link across the skin barrier in a high-performance implantable neuroprosthetic device, such as a visual prosthesis or BMI. Previously, we had described the optimization of the PSC geometries for efficient power transmission based on the

application and fabrication process in an iterative design procedure [11]. Here, we have used a pair of PSCs, optimized in the air at 13.56 MHz, as the foundation for design and optimization of two types of coils for forward data transmission, vertical coils, and figure-8 coils.

Considering that the power carrier of the external transmitter can be up to two orders of magnitude larger than the data carrier, minimization of the power carrier interference on the implanted receiver data coil is of utmost importance. Vertical coils take advantage of the fact that orthogonal coils that are symmetrical ideally have no cross coupling. Figure-8 coils, on the other hand, take advantage of their differential windings to attenuate the effects of any common-mode external electromagnetic field. A detailed comparison between the vertical and figure-8 coils revealed that the former leads to lower interference when coils are perfectly aligned, while the latter is more robust against linear misalignments. With respect to rotations, the results are mixed. Therefore, similar to many other engineering designs, the choice of data coil geometry will depend on the intended application. If the coils' relative positions are going to be stable, such as BMIs, then vertical coils would be better. However, if the coils are expected to move with respect to one another, such as visual prostheses, then Figure-8 coils can result in a more robust system.

Most of the calculations, simulations, and measurement results were in close agreement within the range of parameters needed for neuroprosthetic applications. One major deviation from practical conditions, however, was air as the surrounding medium around the coils, as opposed to neural tissue. The tissue volume conductor will increase the coils' parasitic capacitance and decrease their SRF and quality factors. Therefore, the optimal number of turns and size of the coils are expected to be reduced, particularly for external coils, as we have shown for power PSCs in [18]. On the other hand, since the permeability of tissue is close to that of the air, the difference between k in air and tissue environments will be small. Therefore, the same design criteria that are proposed here will be applicable in the tissue environment.

We are going to use micromachining (MEMS) technology with smaller feature size on high dielectric substrates in order to further shrink the volume of the implantable multiband coil/antenna complex from the present 0.15 cc, and conduct measurements in the real tissue environment.

Acknowledgments

Manuscript received July 23, 2009; revised October 28, 2009 and March 02, 2010. Date of publication June 14, 2010; date of current version September 29, 2010. This work was supported in part by the National Institute of Health grant 1R01NS062031-01A1 and in part by the National Science Foundation under award ECCS-824199.

The authors would like to thank members of the GT-Bionics Lab for their help with the measurements.

References

1. Clark, GM. Cochlear Implants: Fundamentals and Applications. New York: Springer; 2003.
2. Harrison RR, Watkins PT, Kier RJ, Lovejoy RO, Black DJ, Greger B, Solzbacher F. A low-power integrated circuit for a wireless 100-electrode neural recording system. IEEE J Solid-State Circuits. Jan; 2007 42(1):123–133.
3. Humayun MS, Weilanda JD, Fujiia GY, Greenbergb R, Williamsonb R, Littleb J, Mechb B, Cimmarustib V, Boemela GV, Dagneliec G, de Juan E Jr. Visual perception in a blind subject with a chronic microelectronic retinal prosthesis. Vis Res. Nov.2003 43:2573–2581. [PubMed: 13129543]
4. Weiland JD, Liu W, Humayun MS. Retinal prosthesis. Annu Rev Biomed Eng. 2005; 7:361–401. [PubMed: 16004575]

5. Grover, FW. Inductance Calculations: Working Formulas and Tables. New York: Van Nostrand; 1946.
6. Ko WH, Liang SP, Fung CDF. Design of radio-frequency powered coils for implant instruments. Med Biol Eng Comput. Nov.1977 15:634–640. [PubMed: 203785]
7. Zierhofer CM, Hochmair ES. Geometric approach for coupling enhancement of magnetically coupled coils. IEEE Trans Biomed Eng. Jul; 1996 43(7):708–714. [PubMed: 9216142]
8. Harrison RR. Designing efficient inductive power links for implantable devices. Proc IEEE Int Symp Circuits Syst. May.2007 :2080–2083.
9. Yang Z, Liu W, Basham E. Inductor modeling in wireless links for implantable electronics. IEEE Trans Magn. Oct; 2007 43(10):3851–3860.
10. Kim S, Zoschke K, Klein M, Black D, Buschick K, Toepper M, Tathireddy P, Harrison R, Oppermann H, Solzbacher F. Switchable polymer-based thin film coils as a power module for wireless neural interfaces. Sensors Actuators A. May.2007 136:467–474.
11. Jow U, Ghovanloo M. Design and optimization of printed spiral coils for efficient transcutaneous inductive power transmission. IEEE Trans Biomed Circuits Syst. Sep; 2007 1(3):193–202.
12. Normann RA, Maynard EM, Rousche PJ, Warren DJ. A neural interface for a cortical vision prosthesis. Vis Res. Jul.1999 39:2577–2587. [PubMed: 10396626]
13. Ghovanloo M, Atluri S. A wide-band power-efficient inductive wireless link for implantable microelectronic devices using multiple carriers. IEEE Trans Circuits and Systems I, Reg Papers. Oct; 2007 54(10):2211–2221.
14. Takura T, Somekawa T, Sato F, Matsuki H, Sato T. Improvement of communication area for implantable signal transmission system with ferrite chip core. J Appl Phys. Apr.2006 99:08R909.
15. Finkenzeller, K. RFID Handbook: Fundamentals and Applications in Contactless Smart Cards and Identification. 2. New York: Wiley; 2003.
16. Mandal S, Sarpeshkar R. Power-efficient impedance-modulation wireless data links for biomedical implants. IEEE Trans Biomed Circuits Syst. Dec; 2008 2(4):301–315.
17. Kwak SI, Change K, Yoon YJ. Small spiral antenna for wideband capsule endoscope system. Inst Elect Eng Electron Lett. Nov; 2006 42(23):1328–1329.
18. Jow U, Ghovanloo M. Modeling and optimization of printed spiral coils in air, saline, and muscle tissue environments. IEEE Trans Biomed Circuits Syst. Oct; 2009 3(5):339–347. [PubMed: 20948991]
19. Theogarajan LS. A low-power fully implantable 15-channel retinal stimulator chip. IEEE J Solid-State Circuits. Oct; 2008 43(10):2322–2337.
20. Jow U, Ghovanloo M. Optimization of a multiband wireless link for neuroprosthetic implantable devices. Proc IEEE Biomed Circuits and Systems. Nov.2008 :97–100.
21. Nadeem M, Thorlin T, Gandhi OP, Persson M. Computation of electric and magnetic stimulation in human head using the 3-D impedance method. IEEE Trans Biomed Eng. Jul; 2003 50(7):900–907. [PubMed: 12848358]
22. Suzuki N, Nagai Y, Ohtani Y, Ichinose Y. A study on antenna coils for wireless ID tags. Proc Asia-Pacific Microwave Conf. Dec.1997 3:1077–1080.
23. Ghovanloo M, Najafi K. A wideband frequency shift keying wireless link for inductively powered biomedical implants. IEEE Trans Circuits Syst I, Reg Papers. Dec; 2004 51(12):2374–2383.
24. Humayun, MS.; Weiland, JD.; Chader, G.; Greenbaum, E. Artificial Sight: Basic Research, Biomedical Engineering, and Clinical Advances. Vol. ch 9. New York: Springer; 2007.
25. Tang Q, Tummala N, Gupta SKS, Schwiebert L. Communication scheduling to minimize thermal effects of implanted biosensor networks in homogeneous tissue. IEEE Trans Biomed Eng. Jul; 2005 52(7):1285–1294. [PubMed: 16041992]
26. Gabriel S, Lau RW, Gabriel C. The dielectric properties of biological tissues: II. Measurements in the frequency range 10 Hz to 20 GHz. Phys Med Biol. Nov.1996 41:2251–2269. [PubMed: 8938025]
27. *IEEE Standard for Safety Levels With Respect to Human Exposure to Radio Frequency Electromagnetic Fields 3 kHz to 300 GHz*, Std. C95. 1–2005, 2006.

28. Jow U, Ghovanloo M. Modeling and optimization of printed spiral coils in air, saline, and muscle tissue environments. IEEE Trans Biomed Circuits Syst. Oct; 2009 3(5):339–347. [PubMed: 20948991]
29. Grandi G, Massarini A, Kazimierczuk MK, Reggiani U. Stray capacitances of single-layer solenoid air-core inductors. IEEE Trans Ind Appl. Sep./Oct; 1999 35(5):1162–1168.
30. Schantz HS. Introduction to ultra-wideband antennas. Proc IEEE Ultra Wide-Band Systems and Technologies Conf. Nov.2003 :1–9.
31. Milligan, TA. Modern Antenna Design. 2. Hoboken, NJ: Wiley; 2005.
32. Kaiser JA. The Archimedean two-wire spiral antenna. Inst Radio Eng Trans Antennas Propag. May.1960 AP-8:312–323.
33. Alomainy A, Hao Y, Hu X, Parini CG, Hall PS. UWB on-body radio propagation and system modeling for wireless body-centric networks. Proc Inst Elect Eng Commun, Special Issue on UWB, Tech Applications. Feb.2006 153(1)
34. Dissanayake T, Yuce MR, Ho CK. Design and evaluation of a compact antenna for implant-to-air UWB communication. IEEE Antennas Wireless Propag Lett. Apr.2009 8:153–156.
35. Inanlou F, Ghovanloo M. Wideband near-field data transmission using pulse harmonic modulation. IEEE Trans Circuits Syst I, Reg Papers. accepted for publication.
36. Pozar, DM. Microwave Engineering. 2. New York: Wiley; 1998.
37. Oppermann, I.; Hamalainen, M.; Iinatti, J. UWB Theory and Applications. Hoboken, NJ: Wiley; 2004.
38. Andreuccetti, D.; Fossi, R.; Petrucci, C. Dielectric properties of body tissue. [Online]. Available: http://niremf.ifac.cnr.it/tissprop
39. Gosalia K, Humayun MS, Lazzi G. Impedance matching and implementation of planar space-filling dipoles as intraocular implanted antennas in a retinal prosthesis. IEEE Trans Antennas Propag. Aug; 2005 53(8):2365–2373.

Biographies

Uei-Ming Jow: (S'07) received the B.E. degree in electrical engineering from Tatung University, Taipei, Taiwan, in 1999, the M.S. degree in electronic engineering from the

National Taiwan University of Science and Technology, Taipei, in 2001, and is currently pursuing the Ph.D. in electrical and computer engineering at the Georgia Institute of Technology, Atlanta.

From 2001 to 2006, he joined the Industrial Technology Research Institute, Hsinchu, Taiwan, and was an RF Engineer with the Electronics Research and Service Organization. He was involved in the analysis of electromagnetic compatibility for the high-speed digital circuit as well as the embedded radio-frequency circuit packaging technology. His main research interests are neural engineering, bionic systems, integrated analog circuit design, and wireless-implantable biomedical systems.

Maysam Ghovanloo: (S'00–M'04–SM'10) was born in 1973 in Tehran, Iran. He received the B.S. degree in electrical engineering from the University of Tehran, Tehran, Iran, in 1994, the M.S. degree in biomedical engineering from the Amirkabir University of Technology, Tehran, in 1997, and the M.S. and Ph.D. degrees in electrical engineering from the University of Michigan, Ann Arbor, in 2003 and 2004, respectively.

From 2004 to 2007, he was an Assistant Professor in the Department of Electrical and Computer Engineering, North Carolina State University, Raleigh. In 2007, he joined the faculty of Georgia Institute of Technology, Atlanta, where he is currently an Assistant Professor and the Founding Director of the Georgia Tech (GT) Bionics Laboratory in the School of Electrical and Computer Engineering. He has authored or coauthored more than 70 conference and journal publications. Dr. Ghovanloo is an Associate Editor of the IEEE Transactions on Circuits and Systems, Part II: Express Briefs.

Dr. Ghovanloo is the recipient of a CAREER award from the National Science Foundation in 2010. He also received awards in the 40th and 41st Design Automation Conference (DAC)/International Solid-State Circuits Conference Student Design Contest in 2003 and 2004, respectively. He has organized several special sessions and was a member of technical review committees for major conferences in the areas of circuits, systems, sensors, and biomedical engineering. He is a member of the Tau Beta Pi, the Sigma Xi, and the IEEE

Solid-State Circuits Society, the IEEE Circuits and Systems Society, and the IEEE Engineering in Medicine and Biology Society.

Appendix

Rectangular coils' self inductance L was calculated from the following equation by substituting data coil geometries in centimeters [5]

$$\begin{aligned} L=&0.008N_d^2\frac{l_d h_d}{w_d}\\ &\times\left\{\frac{1}{2}\frac{w_d}{h_d}\sinh^{-1}\frac{l_d}{w_d}+\frac{1}{2}\frac{w_d}{l_d}\sinh^{-1}\frac{h_d}{w_d}-\frac{1}{2}\left(1-\frac{h_d^2}{w_d^2}\right)\right.\\ &\times\frac{w_d}{l_d}\sinh^{-1}\frac{l_d}{w_d\sqrt{1+h_d^2/w_d^2}}-\frac{1}{2}\left(1-\frac{l_d^2}{w_d^2}\right)\frac{w_d}{l_d}\\ &\times\sinh^{-1}\frac{h_d}{w_d\sqrt{1+l_d^2/w_d^2}}-\frac{1}{2}\frac{h_d}{w_d}\sinh^{-1}\frac{l_d}{h_d}-\frac{1}{2}\\ &\times\frac{l_d}{w_d}\sinh^{-1}\frac{h_d}{l_d}+\left(\frac{\pi}{2}-\tan^{-1}\frac{l_d h_d}{w_d^2\sqrt{1+g^2/w_d^2}}\right)\\ &+\frac{1}{3}\frac{w_d^2}{l_d h_d}\left[\sqrt{1+\frac{g^2}{w_d^2}}\left(1-\frac{1}{2}\frac{g^2}{w_d^2}\right)+1-\sqrt{1+\frac{l_d^2}{w_d^2}}\right.\\ &\times\left.\left(1-\frac{1}{2}\frac{l_d^2}{w_d^2}\right)-\sqrt{1+\frac{h_d^2}{w_d^2}}\left(1-\frac{1}{2}\frac{h_d^2}{w_d^2}\right)\right]\\ &\left.+\frac{1}{6}\frac{w_d}{l_d h_d}\frac{g^3-l_d^3-h_d^3}{w_d^3}\right\} \end{aligned} \tag{3}$$

in μH, where $g^2=l_d^2+w_d^2$.

Mutual inductance between a pair of rectangular solenoids was calculated by making adjustments in the circular solenoid equations from [5]

$$M=0.001(A_3)(A_4)\frac{N_3}{W_{d3}}\cdot\frac{N_4}{W_{d4}}\cdot\left[\frac{Z_1}{r_1}-\frac{Z_2}{r_2}-\frac{Z_3}{r_3}+\frac{Z_4}{r_4}\right] \tag{4}$$

where

$$\begin{aligned} &A_3=(l_{d3}\cdot h_{d3}),\ A_4=(l_{d4}\cdot h_{d4}),\ \text{and}\\ Z_m=&T_2t_2-\frac{1}{4}\frac{h_{d3}^2}{r_m^2}\left(T_4t_2+\frac{h_{d4}^2}{h_{d3}^2}T_2t_4\right)P_2(\mu_m)+\frac{1}{8}\frac{h_{d3}^4}{r_m^4}\\ &\times\left(T_6t_2+3\frac{h_{d4}^2}{h_{d3}^2}T_4t_4+\frac{h_{d4}^4}{h_{d3}^4}T_2t_6\right)P_4(\mu_m)-\frac{5}{64}\frac{h_{d3}^6}{r_m^6}\\ &\times\left(T_8t_2+6\frac{h_{d4}^2}{h_{d3}^2}T_6t_4+6\frac{h_{d4}^4}{h_{d3}^4}T_4t_6+\frac{h_{d4}^6}{h_{d3}^6}T_2t_8\right)P_6(\mu_m)\\ &+\frac{7}{128}\frac{h_{d3}^8}{r_m^8}\left(T_{10}t_2+10\frac{h_{d4}^2}{h_{d3}^2}T_8t_4+20\frac{h_{d4}^4}{h_{d3}^4}T_6t_6\right.\\ &\left.+10\frac{h_{d4}^6}{h_{d3}^6}T_4t_8+\frac{h_{d4}^8}{h_{d3}^8}T_2t_{10}\right)P_8(\mu_m)+\ldots \end{aligned}$$

in microHenries. The four radii vectors r_m (m = 1 to 4), depend on the four distances d_m given by

$$r_m=\sqrt{d_m^2+(D+h_{d3}/2+h_{d4}/2)^2},$$
$$d_1=X-\left(\frac{W_{d4}+W_{d3}}{2}\right),\quad d_2=X+\left(\frac{W_{d4}-W_{d3}}{2}\right),$$
$$d_3=X+\left(\frac{W_{d3}-W_{d4}}{2}\right),\quad d_4=X+\left(\frac{W_{d3}+W_{d4}}{2}\right).$$

$\mu_m = d_m/r_m$, and $P_{2n}(\mu_m)$ (n is a positive integer) are known as zonal harmonics, given by [5]

$$P_{2n}(\mu_m)=\frac{(2\cdot 2n-1)(2\cdot 2n-3)\ldots 1}{(2n)!}\times\left[\mu_m^{2n}-\frac{2n(2n-1)}{2(2\cdot 2n-1)}\mu_m^{2n-2}+\frac{2n(2n-1)(2n-2)(2n-3)}{2\cdot 4(2\cdot 2n-1)(2\cdot 2n-3)}\mu_m^{2n-4}-\ldots\right]. \quad (5)$$

T_2 and t_2 are a function of $Dia_3^2/(h_{d3}/2)^2$ and $Dia_4^2/(h_{d4}/2)^2$, respectively, and the same is true for T_4 and t_4, T_6 and t_6, so on and so forth. The coefficients t_2, t_4, t_6,… or T_2, T_4, T_6,… are functions of the ratio τ of the height of the coil (h_d) and its mean wire diameter (Dia).

For the external coil, L3 $(T_n)\tau_{ex}^2=Dia_3^2/(h_{d3}/2)^2$.

For internal coil, L4 (t_n) $\tau_{in}^2=Dia_4^2/(h_{d4}/2)^2$

$$T_n \text{ or } t_n=1+\frac{n(n-1)}{3!}\frac{\tau^2}{2^2}+\frac{n(n-1)(n-3)}{5!}\frac{\tau^4}{2^4}+\ldots+\frac{n(n-1)(n-3)\ldots[n-(n-1)]}{(n+1)!}\frac{\tau^n}{2^n}.$$

Finally, by substituting L and M from the aforementioned equations in (1), k_{34} can be found.

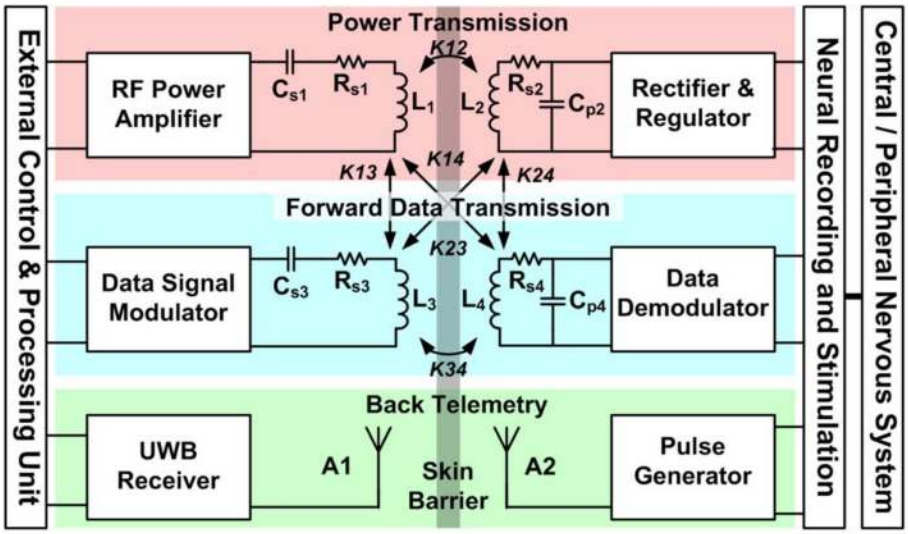

Fig. 1.
Block diagram of the multiband wireless link and its associated blocks in a high-performance implantable neuroprosthetic device [20].

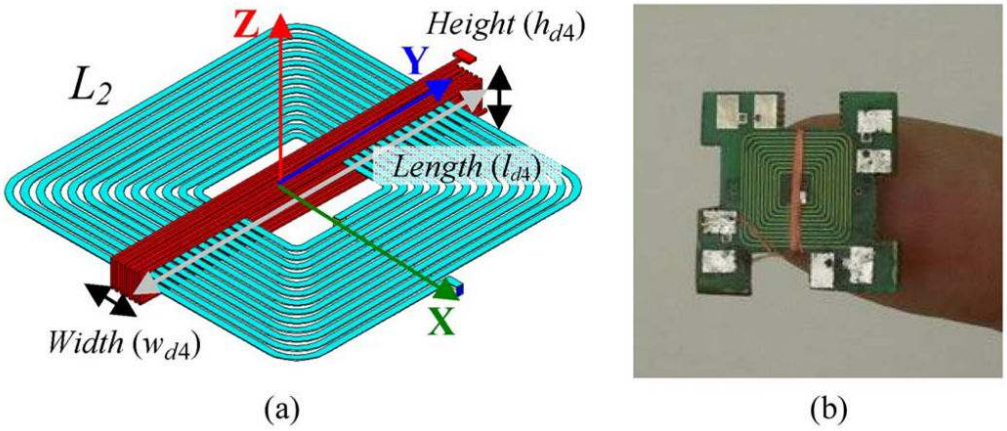

Fig. 2.

(a) Rendering of the power and forward data transmission coils, showing their important geometrical parameters. (b) Receiver data and power coils fabricated on a four-layer printed-circuit board (FR4) [20].

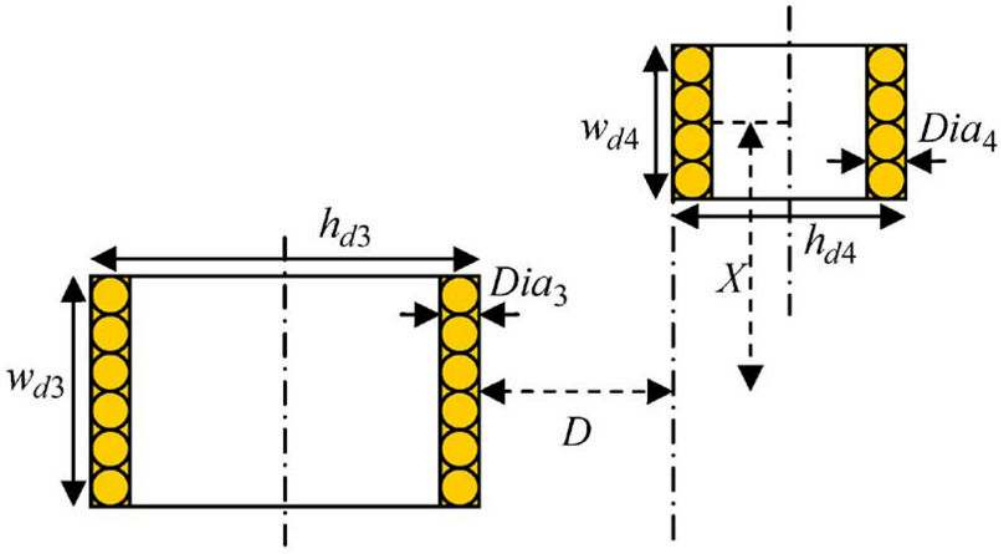

Fig. 3.
Cross-sectional view of a pair of coupled solenoid inductors [5].

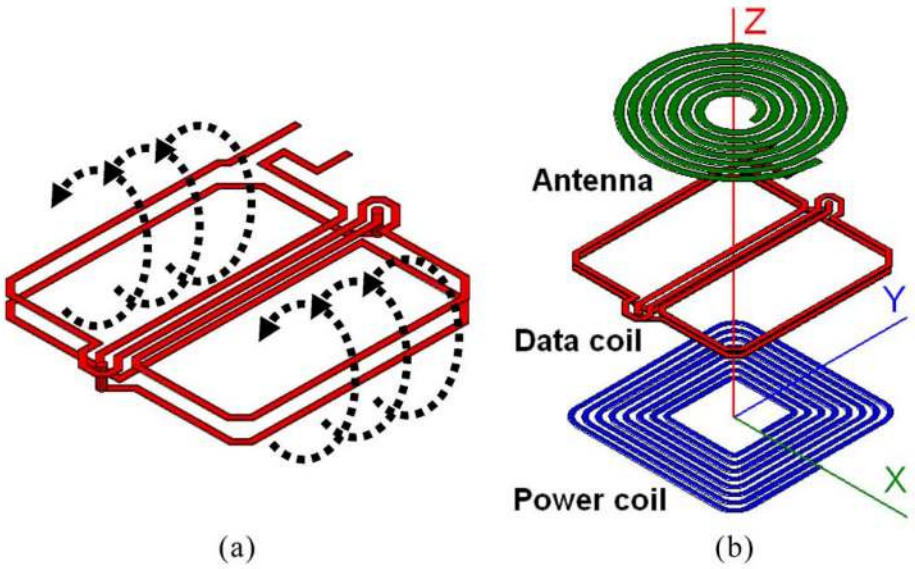

Fig. 4.
(a) Planar figure-8 coil layout. (b) Exploded view of the UWB antenna stacked on top of the power PSC and figure-8 data coil in a four-layer PCB to form the implantable side of the multiband wireless link ($10 \times 10 \times 1.5$ mm^3).

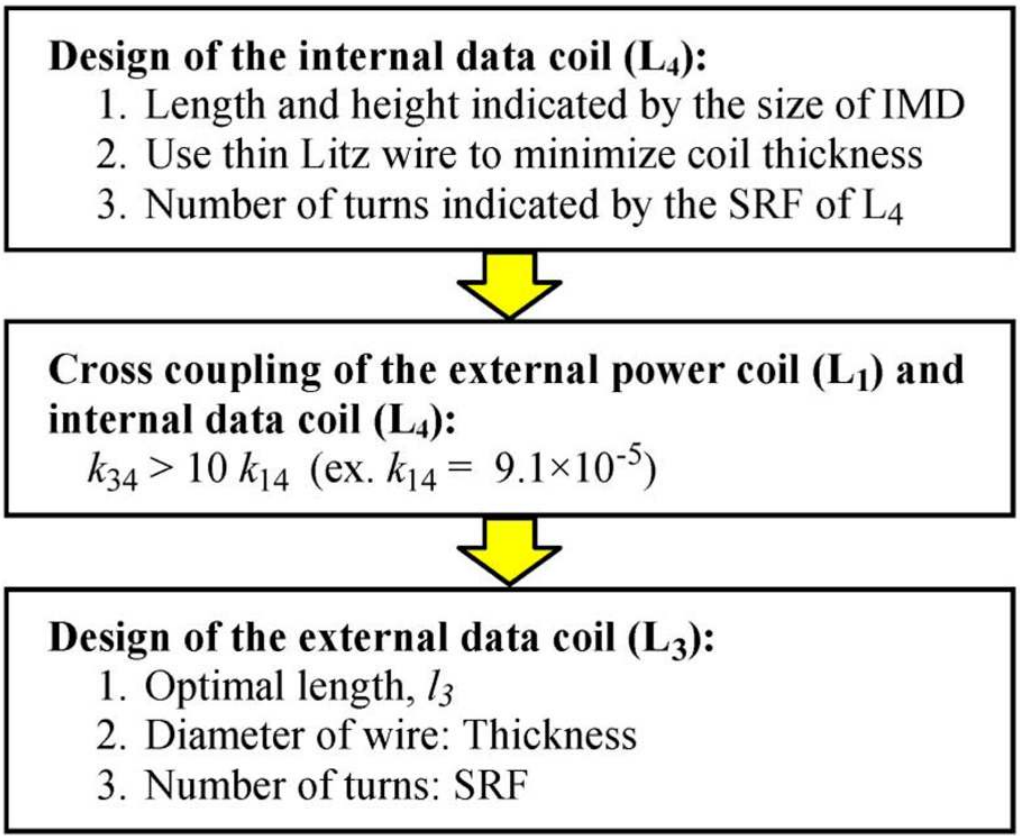

Fig. 5.
Design procedure for the optimal design of the vertical data coils.

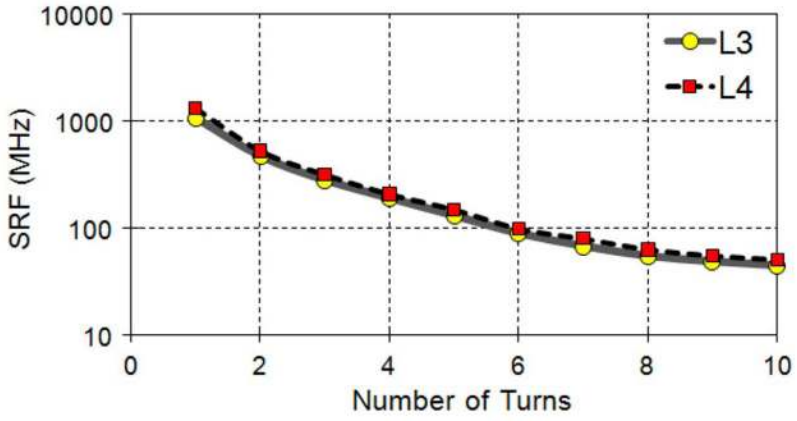

Fig. 6.
Self-resonance frequency versus number of turns for the vertical data coils.

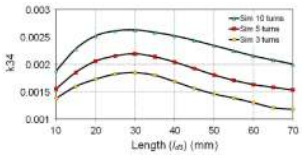

Fig. 7.
Vertical data coils direct coupling as a function of the length of L_3 when the coils are 10 mm apart.

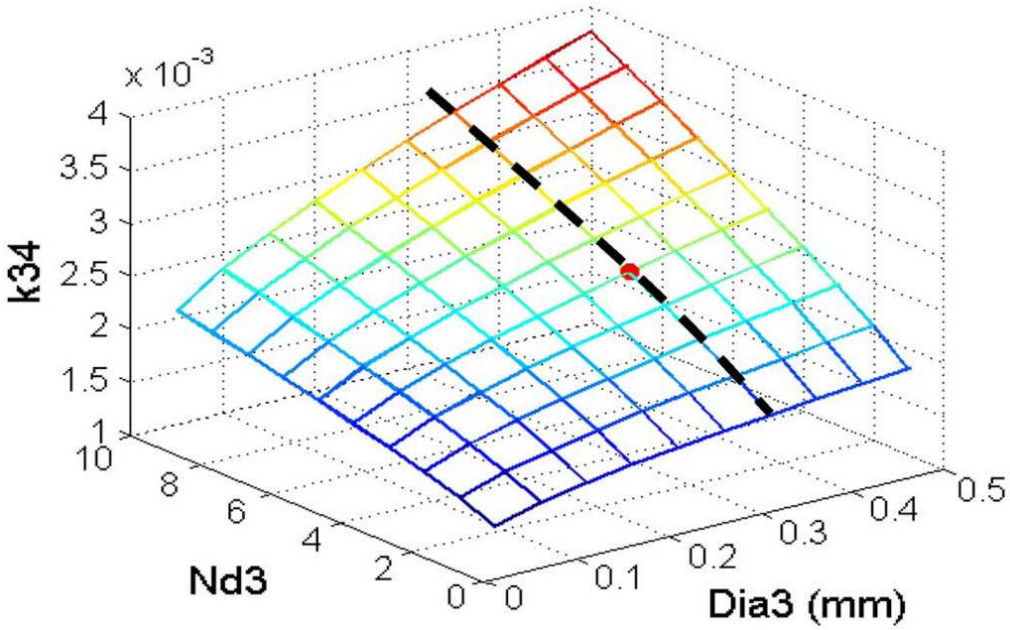

Fig. 8.

Effects of varying the number of turns and the wire diameter of the external data coil (L_3) on data coils direct coupling, k_{34}.

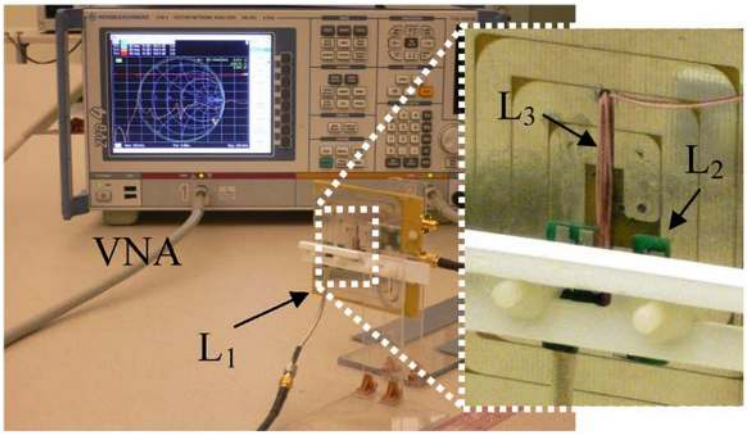

Fig. 9.
Setup for direct- and cross-coupling measurements. Inset: the relative position of the external power (L_1) and vertical data coils (L_3) with respect to implantable coils (L_2 and L_4), which are also shown separately in Fig. 2(b).

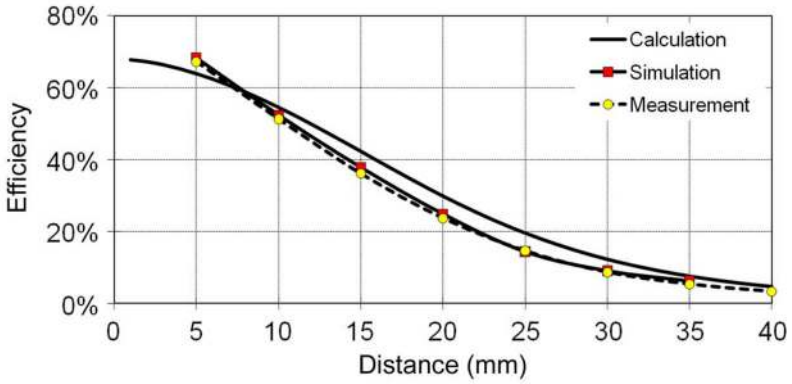

Fig. 10.
Calculated, simulated, and measured efficiency variations with coils relative distance *D* for power PSCs in Table II at 13.56 MHz [11].

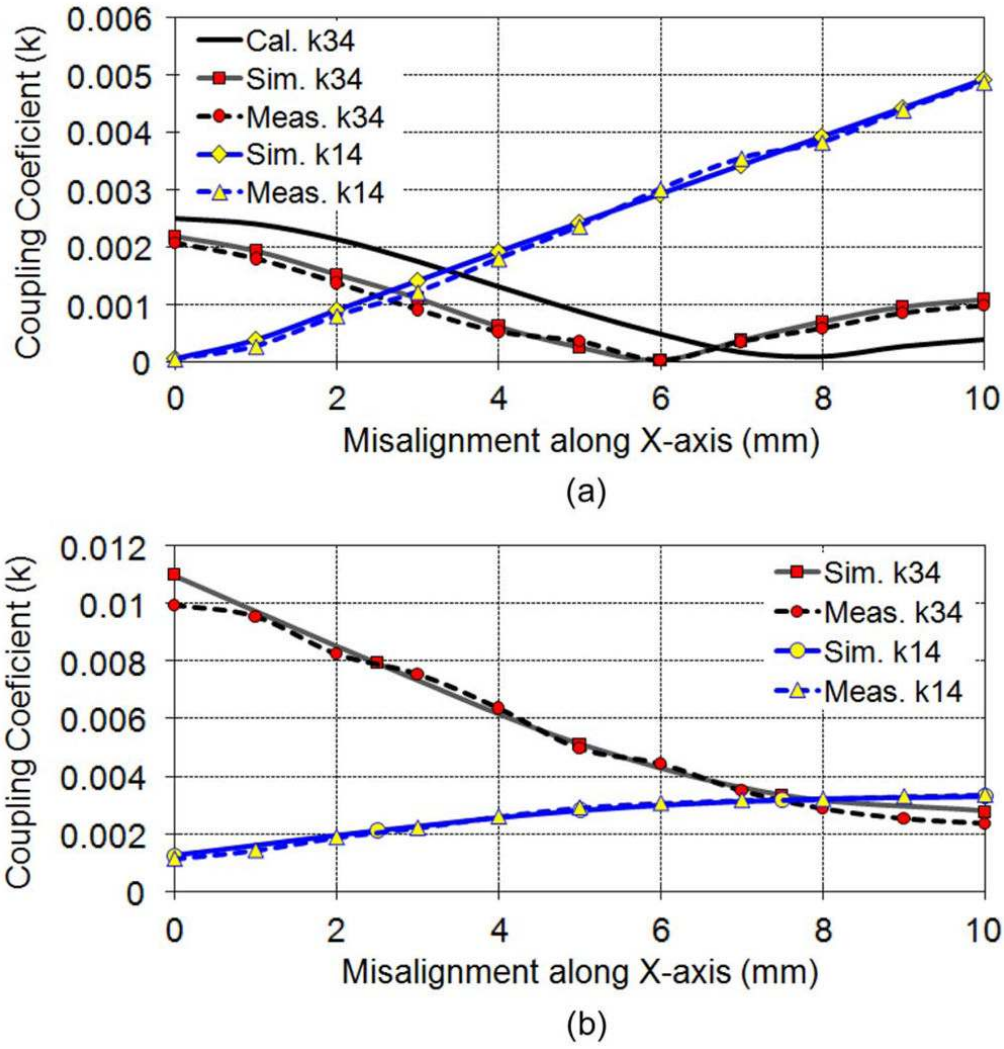

Fig. 11.

(a) Calculation (see Appendix), simulation, and measurement of vertical data coils' direct coupling (k_{34}) and cross coupling with power PSCs (k_{14}) versus misalignment along the X-axis (see Fig. 2(a)). (b) Simulation and measurement of figure-8 data coils'k_{34} and k_{14} versus misalignment along the X-axis [see Fig. 8(b)]. The coils' relative distance is maintained at D = 10 mm.

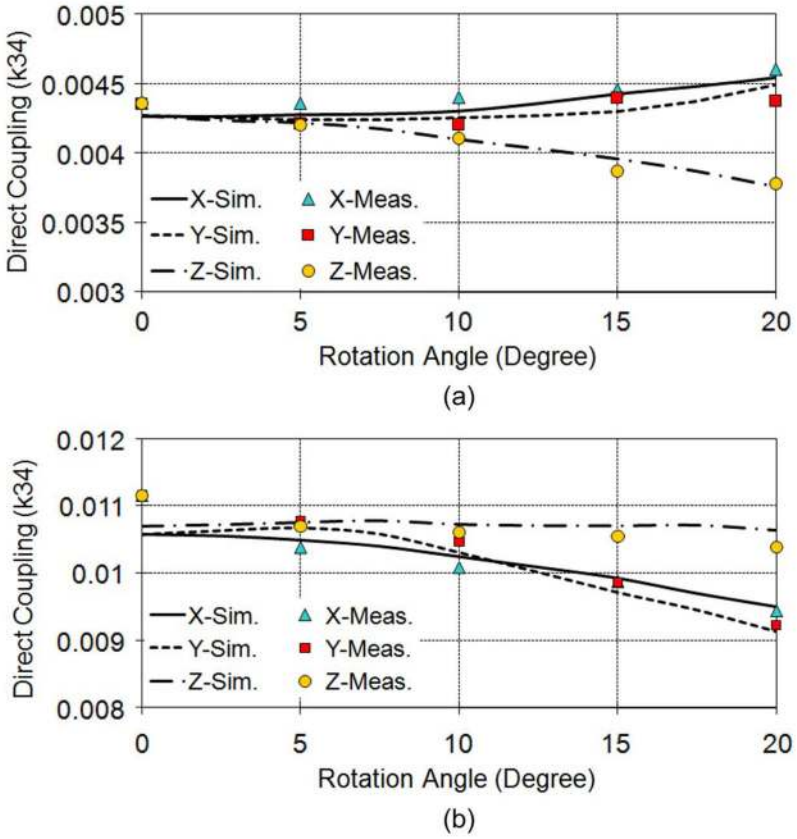

Fig. 12.

(a) Simulation and measurement results of the vertical data coils direct coupling (k_{34}) versus rotation angle of L_3 pivotal to the X-, Y-, and Z-axes, while maintaining a center-to-center spacing of D = 10 mm. (b) Similar simulation and measurement results for figure-8 data coils.

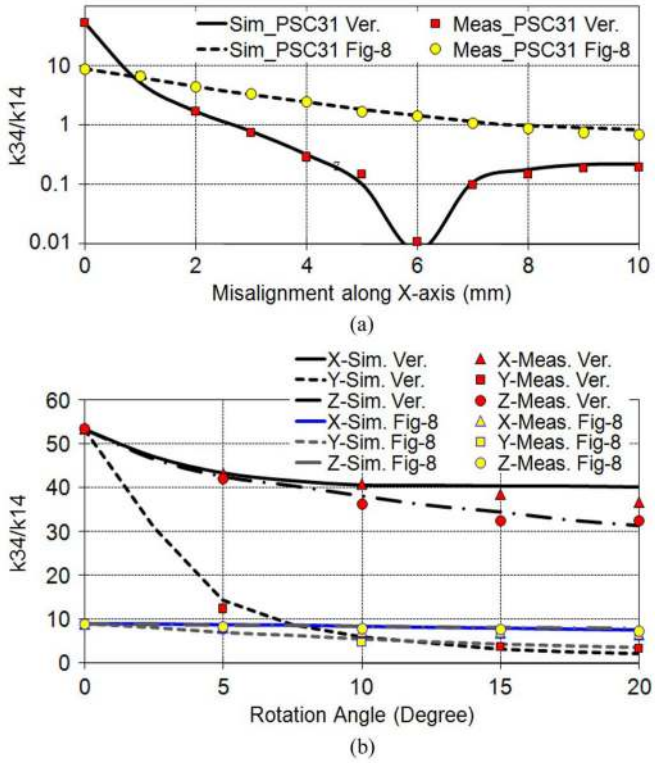

Fig. 13.

(a) Comparing the k_{34}/k_{14} ratio between vertical and figure-8 data coils versus linear misalignment along the X-axis. (b) Comparing k_{34}/k_{14} be-tween vertical and figure-8 coils versus rotations. The coils' relative distance is kept at D = 10 mm.

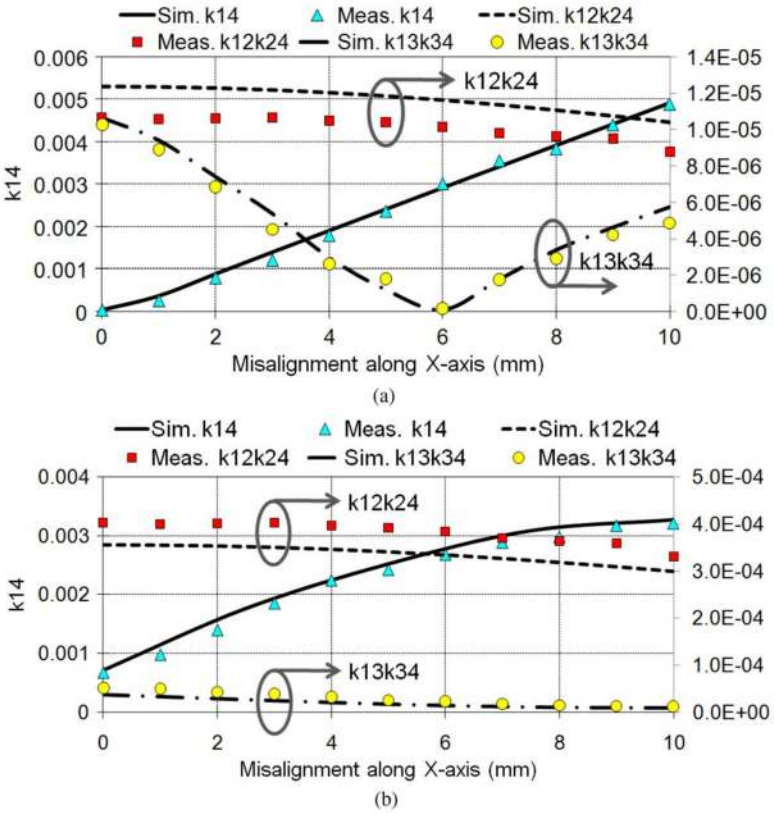

Fig. 14.

(a) Calculation (see Appendix), simulation, and measurement of the effect of misalignment along the X-axis on indirect coupling paths in vertical data coils [see Fig. 2(a)]. (b) Effect of misalignment along the X-axis on indirect coupling paths in figure-8 data coils [see Fig. 4(b)]. The coils' relative distance is maintained at D = 10 mm.

Fig. 15.
Simulation and measurement of S_{11} with and without the vertical data coil for the UWB spiral antenna, A_2, that is implemented on the same PCB as L_2 and figure-8 L_4, as shown in Fig. 4(b).

TABLE I

Design Constrains Imposed by the Application and Fabrication Process

Parameter	Symbol	Design Value
Implanted PSC outer side	d_{o2}	10 mm
PSCs relative nominal distance	D	10 mm
Power carrier frequency	f_P	13.56 MHz
Secondary nominal loading	R_l	500 Ω
Conductor thickness	t_c	38 μm
PCB substrate thickness	t_s	1.5 mm
PCB substrate dielectric constant	ε_{rs}	FR4, 4.4

TABLE II

Optimized Power PSC Geometries and Specifications

Parameter	L_1	L_2	Parameter	L_1	L_2
d_o (mm)	79	10	w (μm)	5500	290
d_i (mm)	11.2	2.96	s (μm)	150	150
ϕ (fill factor)	0.751	0.543	L (μH)	1.22	0.49
n (turns)	6	8	Q	102	36
Frequency (MHz)	13.56				
k_{12}	0.036				
Efficiency (%)	56.65 (with perfect alignment)				

* Derived from using Table I in the iterative procedure explained in [11].

IEEE Trans Biomed Circuits Syst. Author manuscript; available in PMC 2011 September 12.

TABLE III

Optimized Vertical Data Coil Characteristics

Parameter	L_3	L_4
Type of Litz wire	7 × AWG-36	7 × AWG-48
Wire Diameter (μm)	350	100
Number of Turns	5	6
Length (mm)	30	10.2
Width (mm)	2.0	1.0
Height (mm)	2.2	1.7
Inductance (μH)*	0.3081	0.5972
SRF (MHz)*	128.8	98.8
C_{s3} and C_{p4} (pF)	58.46	27.9
Q @ 50 MHz*	50.2	20.2
k_{34}*	0.0022	

*Simulated in the HFSS.

TABLE IV

Optimized Figure-8 Data Coil Characteristics

Parameter	L_3	L_4
Line width (mm)	2	0.2
Size (mm^2)	32 × 32	10 × 10
Number of turns	2	2
Inductance (μH)*	0.1306	0.3338
SRF (MHz)*	138	256
C_{s3} and C_{p4} (pF)	137.9	52.80
Q @ 50 MHz*	46.4	38.8
k_{34}*	0.011	

*Simulated in the HFSS.